

PHOTONICS Research

Highly tunable optical response in dielectric-embedded plasmonic nanocavities

JUNSHENG ZHENG,^{1,2} ALEXEY V. KRASAVIN,³ ZHIYONG LI,^{1,2,4} D XIN GUO,^{1,2,4} ANATOLY V. ZAYATS,³ D LIMIN TONG.^{1,2,5} AND PAN WANG^{1,2,4,5,*} D

¹New Cornerstone Science Laboratory, State Key Laboratory of Extreme Photonics and Instrumentation,

College of Optical Science and Engineering, Zhejiang University, Hangzhou 310027, China

Received 22 April 2025; revised 22 June 2025; accepted 22 June 2025; posted 24 June 2025 (Doc. ID 565888); published 28 August 2025

Developing approaches for precise engineering of the optical response of plasmonic nanocavities at the post-fabrication stage is important for achieving enhanced and tunable light-matter interactions. In this work, we demonstrate selective enhancement/suppression of specific plasmonic modes by embedding nanocube-on-mirror plasmonic nanocavities into a poly(methyl methacrylate) (PMMA) layer with a controllable thickness. With the increase of the PMMA thickness from 0 to approximately 100 nm, the dominating out-of-plane plasmonic modes are significantly suppressed in the scattering spectra, while the in-plane plasmonic modes are greatly enhanced with a factor reaching 102 ± 20 . This enhancement is related to the variation of momentum matching between the plasmonic modes and the radiative fields, affecting both mode excitation and emission properties. In addition, the spectral positions of the in-plane and out-of-plane plasmonic modes shift up to 52 ± 5 and 81 ± 2 nm, respectively. These properties are important for matching and enhancing plasmonic and molecular resonances in a variety of applications.

Published by Chinese Laser Press under the terms of the Creative Commons Attribution 4.0 License. Further distribution of this work must maintain attribution to the author(s) and the published article's title, journal citation, and DOI. https://doi.org/10.1364/PRJ.565888

1. INTRODUCTION

Metal nanostructures have attracted significant attention during the past decades due to their ability to support localized surface plasmon resonances that can confine electromagnetic fields down to a deep-subwavelength scale and provide significant local-field enhancement [1,2]. They have led to many advances in both fundamental nanophotonic research and development of a variety of applications ranging from bio- or chemical sensing [3-5] and plasmon-enhanced spectroscopy [6-8] to nanophotonic devices (e.g., nanolasers and high-speed optical modulators) [9,10]. Recently, nanoparticle-on-mirror (NPoM) nanocavities, which can be readily fabricated by depositing metal nanoparticles onto a metal mirror covered with a nanometer-thick dielectric layer, have been intensely studied because of their ability to squeeze electromagnetic fields down to the single-nanometer or even sub-nanometer scale [11–14]. Therefore, they provide an unmatched nanophotonic platform for the study of light-matter interaction on the atomic scale, opening a new realm of possibilities for a broad range of applications including single-molecule strong coupling [15], enhancement of forbidden transitions [16,17], and nanoscale optoelectronic devices [18].

Due to the strong electromagnetic coupling between the metal nanoparticle and the mirror, NPoM nanocavities can support a rich variety of plasmonic modes across a broad spectral range [19,20]. In general, it is highly desired to selectively excite/enhance and precisely tune these modes to achieve the best performance of NPoM nanocavities for particular applications. For example, tuning a spectral position of a resonance mode to target the emission wavelength of emitters integrated in the nanocavity (e.g., dyes, rare-earth ions, or quantum dots) can be used to maximize the Purcell effect [21,22], while enhanced excitation of the specific resonance mode can promote selective interaction with the desired electronic state of matter (e.g., excitons) [23,24]. Theoretically, the optical response of plasmonic nanocavities can be precisely controlled by adjusting the size and shape of the nanoparticles, the thickness of the

²Zhejiang Key Laboratory of Optoelectronic Information Technology, Zhejiang University, Hangzhou 310027, China

³Department of Physics and London Centre for Nanotechnology, King's College London, London WC2R 2LS, UK

⁴Jiaxing Key Laboratory of Photonic Sensing and Intelligent Imaging, Intelligent Optics and Photonics Research Center,

Jiaxing Research Institute, Zhejiang University, Jiaxing 314000, China

⁵Collaborative Innovation Center of Extreme Optics, Shanxi University, Taiyuan 030006, China

^{*}Corresponding author: nanopan@zju.edu.cn

dielectric layers and metal mirrors, as well as the excitation conditions (e.g., the incident angle and polarization of the incident light) [12,19,25,26]. However, due to extreme sensitivity of the strongly confined optical fields in NPoM nanocavities to their structural parameters, in practice, it is challenging to obtain NPoM nanocavities whose optical response is the same as the desired. Therefore, an approach for precise engineering of the optical response of NPoM nanocavities at the postfabrication stage is highly desirable. Several methods have been developed towards this goal, including laser-induced reshaping of the metal nanoparticles in order to enrich the supported plasmonic modes [27] or integrating an active layer with an electrically tunable refractive index into the nanocavity gap to tune the mode resonance wavelengths [28,29]. However, the former approach usually results in an irreversible alteration to the metal nanoparticles and a potential damage to the functional materials frequently integrated into the gap, while the latter shows only limited tunability.

Here, we demonstrate precise control of the plasmonic response of nanocube-on-mirror (NCoM) plasmonic nanocavities by embedding them into a poly(methyl methacrylate) (PMMA) layer with a variable thickness. Single-crystal gold nanocubes (~60 nm in size) and flakes were used to construct the NCoM nanocavities with low loss and uniform spectral response. As the PMMA thickness increases from 0 to approximately 100 nm, the dominant out-of-plane plasmonic

modes are markedly suppressed and eventually vanish from the scattering spectrum, while the in-plane plasmonic modes are significantly enhanced, with their intensity increasing by a factor of ~100. This enhancement stems from the variation of momentum matching between the plasmonic modes and the radiative fields, affecting both mode excitation and emission properties, as confirmed by the theoretical simulation results. In addition, the resonant peak wavelengths of the in-plane and out-of-plane plasmonic modes are tuned up to ~52 and 81 nm, respectively.

2. FABRICATION AND CHARACTERIZATION OF NCOM PLASMONIC NANOCAVITIES

In order to obtain plasmonic nanocavities with low loss and uniform spectral response, chemically synthesized single-crystal gold nanocubes with high uniformity in size [30] and gold flakes with an ultrasmooth surface (having a typical surface root-mean-square roughness of ~0.2 nm [19,31]) are used as building blocks for the construction of the NCoM plasmonic nanocavities [18], as shown in Fig. 1(a) (see Appendix A for the fabrication details). Figure 1(b) presents a cross-sectional transmission electron microscopy (TEM) image of an individual NCoM nanocavity (see Appendix B), clearly showing that the gold nanocube (~60 nm in size) and the gold flake (~50 nm in thickness) are well separated by a dielectric layer,

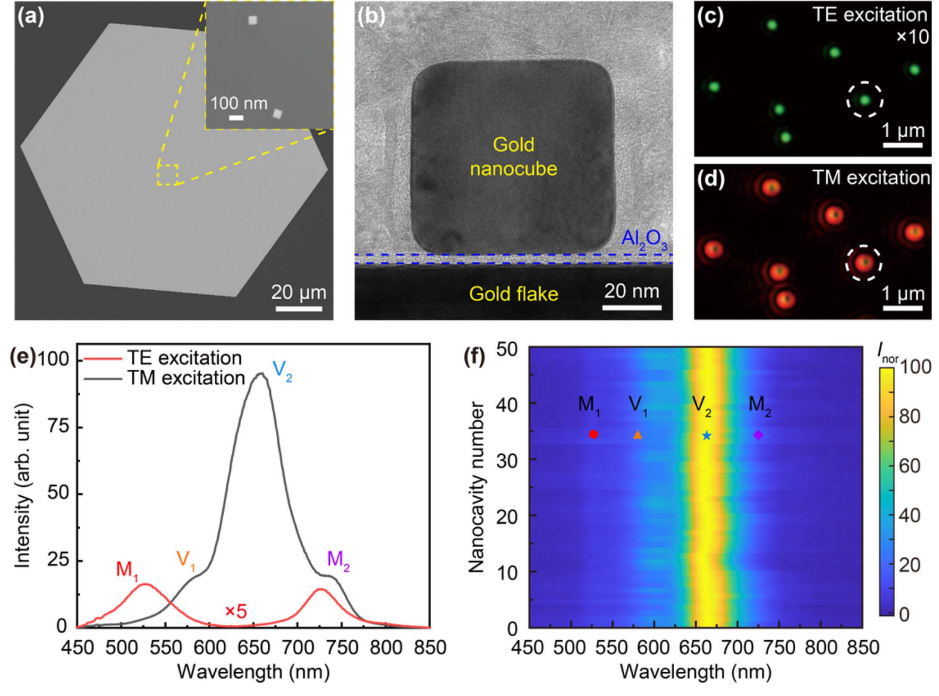


Fig. 1. Characterization of single NCoM plasmonic nanocavities. (a) Scanning electron microscopy image of a single-crystal gold flake (covered with a 2.5-nm-thick alumina layer) with gold nanocubes deposited onto it (as shown in the inset) to form NCoM plasmonic nanocavities. (b) Cross-sectional TEM image of an NCoM plasmonic nanocavity with a gap consisting of a 1.8-nm-thick CTAB bilayer and a 2.5-nm-thick alumina layer. Note that the CTAB layer capping the gold nanocube cannot be observed because it was destroyed during the preparation of the cross-sectional lamella. The blue dashed lines indicate the outlines of the alumina layer. (c), (d) Dark-field scattering images of NCoM plasmonic nanocavities in air taken under TE (c) and TM (d) excitation conditions. (e) Experimentally measured scattering spectra of the nanocavity encircled in (c) and (d) under TE (red line) and TM (black line) excitation conditions. (f) Measured scattering spectra of 50 nanocavities formed on the same gold flake under unpolarized light illumination. The solid dot, triangle, star, and rhombus represent the resonance wavelengths of modes M_1, M_2, V_1 , and V_2 , respectively, marked in (e). I_{nor} represents the normalized scattering intensity.

which consists of a 1.8-nm-thick bilayer of cetyltrimethylammonium bromide (CTAB) capping the nanocubes and a 2.5-nm-thick alumina spacer deposited on the flake. Under the illumination with a TE- and TM-polarized white light at the angle of incidence of 80° (see Appendix C for the experimental details) [32-34], the nanocavities exhibit uniform green [Fig. 1(c)] and doughnut-shaped red [Fig. 1(d)] scattering, respectively. Particularly, under the TE-polarized illumination, there are two resonance peaks located at the wavelengths of 527 and 725 nm in the scattering spectrum [labeled as M_1 and M_2 , respectively; red line in Fig. 1(e)]. The observed modes are reproduced very well in the simulated scattering spectrum and correspond to the flake-coupled quadrupolar and transversal dipolar modes of the nanocube, respectively (see Appendix D for the simulated scattering spectrum and the corresponding charge density distributions) [19,20]. These two modes are poorly coupled to light and therefore can be regarded as dark. They are excited by the in-plane component of the electric field. Under the TM-polarized illumination, another two scattering peaks located at the wavelengths of 581 and 660 nm appear [labeled as V₁ and V₂, respectively; black line in Fig. 1(e)], which stem from hybridization of the flake-coupled vertical dipolar mode of the nanocube and one of the second-order metal-insulator-metal (MIM) modes in the nanocavity gap (see Appendix D for the corresponding charge density distributions) [19,20,35]. Different from modes M₁ and M₂, these two modes are bright and preferably excited by the out-of-plane component of the electric field. In addition, the slight difference in the peak wavelengths for mode M₂ under TE and TM excitations arises from a slight difference in the in-plane edge lengths of the nanocube. Benefiting from the excellent structural quality of the plasmonic building blocks and the uniform thickness of the deposited alumina layer, the as-fabricated NCoM nanocavities show uniform plasmonic resonances in the scattering spectra [Fig. 1(f)].

3. ENGINEERING OF PLASMONIC RESONANCES

The optical response of the NCoM plasmonic nanocavities can be readily engineered by embedding them into a dielectric layer with a controllable thickness. Experimentally, it is realized by first spin-coating a 96-nm-thick PMMA layer onto the NCoM nanocavities (to ensure the complete embedding), and then using O_2 plasma etching to gradually tune its thickness (d_p) , as schematically shown in Fig. 2(a) (see Appendix A for the fabrication details). The thickness in this case can be precisely controlled with a precision of ± 3 nm by setting the treatment time and referring to the thickness-etching time correlation curve of the PMMA layer [as presented in Fig. 2(b); see Appendix E for the measurement details]. In the case of over-etching, the PMMA layer can be etched completely first, and a new PMMA layer (~96 nm) can be spin-coated onto the same nanocavities and then etched to readjust the PMMA thickness. Their relative positions and optical response remain unchanged after several rounds of spin-coating and etching of PMMA layer (see Appendix F for details). As a result, the evolution of the scattering spectrum of a PMMA-embedded NCoM nanocavity can be obtained by progressively decreasing

the PMMA thickness d_p , as shown in Figs. 2(c) and 2(d). In the case of TE-polarized light illumination when only modes M₁ and M_2 are excited, with the decrease of d_p , the resonance wavelengths of the modes are gradually blue-shifted. This is accompanied by a decrease of their scattering intensities, which can be intuitively seen on the dark-field scattering images shown in the lower panels in Fig. 2(c). Under the excitation with TM-polarized light, modes M₁ and M₂ dominate the scattering spectrum for the thicknesses of the PMMA layer above ~50 nm, while with further decrease of the thickness, modes V₁ and V₂ appear and their scattering intensities drastically increase (especially that for mode V₂). The corresponding darkfield scattering images [lower panels in Fig. 2(d)] demonstrate the trends observed in the spectra, with the red doughnutshaped component (corresponding to mode V₂) gradually appearing with the decrease of the PMMA thickness under the TM excitation, and then dominating the pattern for the thin (less than 36 nm) PMMA layers. With the decrease of d_p , the resonance wavelengths of modes M_1, M_2 , and V_2 also gradually blue-shift. At the same time, mode V₁, which is less radiative in nature for its anti-bonding characteristic, is only observable when the thickness of the PMMA layer is below 36 nm due to the spectral mismatch between the vertical dipolar mode of the nanocube and the second-order MIM mode in the gap for thicker PMMA layers [35].

To get an insight into the effect of the thickness of the PMMA layer on the optical response, finite element numerical simulations of light scattering on NCoM nanocavities embedded in a PMMA layer with a varied thickness were performed. Figures 3(a) and 3(b) present the calculated scattering spectra under TE-polarized and TM-polarized light illuminations, respectively, and consistently reproduce the experimental observations [Figs. 2(c) and 2(d)]. The spectral positions and scattering intensity enhancement of the plasmonic resonances extracted from the experimental and calculated scattering spectra for modes M₁, M₂, V₁, and V₂ are then quantitatively compared in Figs. 3(c)–3(e). The scattering peak intensity ratio is defined as I_p/I_0 , where I_p and I_0 are the peak scattering intensities of the plasmonic modes for NCoM nanocavities with various PMMA thicknesses d_p and that without the PMMA layer, respectively. As discussed above, for mode M_1 , with the increase of d_p from 0 to 96 nm, its resonance wavelength experiences a gradual red-shift from 525 to 578 nm, while for mode M₂ a visible red-shift from 727 to 768 nm only occurs when d_p is less than 48 nm [Fig. 3(c), solid dots]. This is understandable because for mode M₂ the electromagnetic energy is mostly confined in the nanocavity gap, while for mode M₁ the electromagnetic energy is confined not only in the nanocavity gap but also around the top surface of the nanocube, which can be clearly seen on the corresponding near-field maps shown in Figs. 4(a), 4(b), 4(d), and 4(e). The calculated evolutions of the resonance wavelengths reproduce the experimental results very well [Fig. 3(c), dashed lines]. More interestingly, with the increase of d_p from 36 to 84 nm, there is a significant enhancement of the peak scattering intensity for mode M₁; the measured scattering peak intensity ratio reaches a maximum value of 102 ± 20 when d_p is 84 nm [Fig. 3(d)]. The slight difference between the experimental

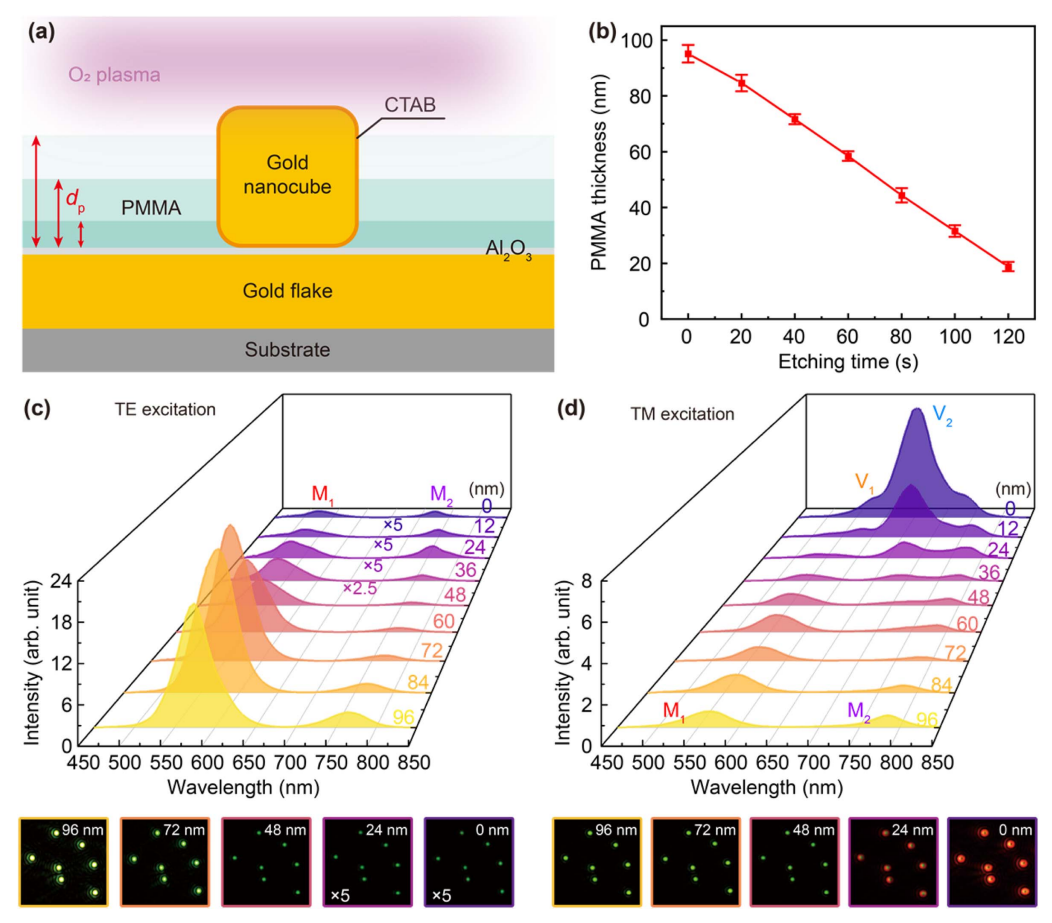


Fig. 2. Effect of PMMA layer thickness on plasmonic resonances of NCoM nanocavities. (a) Schematical illustration of precise control of the thickness of the PMMA layer surrounding an NCoM plasmonic nanocavity via O₂ plasma etching. (b) Measured thickness-etching time correlation curve of the PMMA layer. (c), (d) Measured dark-field scattering spectra of an individual NCoM plasmonic nanocavity embedded in a PMMA layer with a varying thickness under TE (c) and TM (d) excitation conditions. Lower panels show the corresponding dark-field scattering images of the nanocavity for various thicknesses of the PMMA layer.

and calculated results may occur due to the additional surface roughness of the PMMA layer introduced by the O₂ plasma etching used in the experiments. Mode M₁ with electromagnetic energy confined also around the top surface of the nanocube is sensitive to the surface roughness of the PMMA layer, resulting in an enhancement in the scattering of near-field electromagnetic energy into the far field. The significant enhancement in the scattering intensity of mode M₁ with an increase of the PMMA thickness can be attributed to the simultaneous rise of the excitation and out-coupling efficiencies. On one hand, the increase of the surrounding refractive index leads to the increase of the wave number of the incident light, which enlarges the field retardation effects, and therefore boosts the excitation efficiency of mode M1 (which, as noted above, originates from the coupling of a quadrupolar mode of the nanocube with the gold flake) [36,37], as shown in Figs. 4(a) and 4(b). On the figure one can observe that the retardation-induced effects lead to an ~200% enhancement of the excited mode electric field (defined as a ratio between the local |E| and incident $|E_0|$ electric fields). On the other hand, the increase in the surrounding refractive index exploiting the same retardation effects also reduces the momentum

mismatch between the mode highly confined in the nanocavity gap and the free-space light, which results in an increase of the mode radiation efficiency [38]. The latter phenomenon was confirmed by calculation of radiation efficiency for modes M₁ and M₂ using eigen-mode simulations, which were performed using built-in eigen-frequency [the radiation efficiency was calculated as $P_r/(P+P_{abs})$, where P_r , P_r , and $P_{\rm abs}$ represent far-field power flow inside a 64° collection angle corresponding to the NA of the objective, and total far-field power flow and absorbed power, respectively, for NCoMs with various PMMA thicknesses d_p ; see Appendix D for the simulation details]. The radiation efficiency for mode M₁ increases from 0.8% to 23.1%, reaching a maximum enhancement value of ~29 at $d_p = 96$ nm [Fig. 4(c)], which confirms that the out-coupling efficiency is another important factor for the scattering intensity enhancement. Comparing the excitation and radiation efficiencies with the theoretical scattering enhancement of \sim 56, one can conclude that for mode M_1 the radiation enhancement plays the major role.

With the increase of d_p from 0 to 96 nm, the peak scattering intensity of mode M_2 shows a similar trend to that of mode M_1 , but with a significantly reduced enhancement factor, which

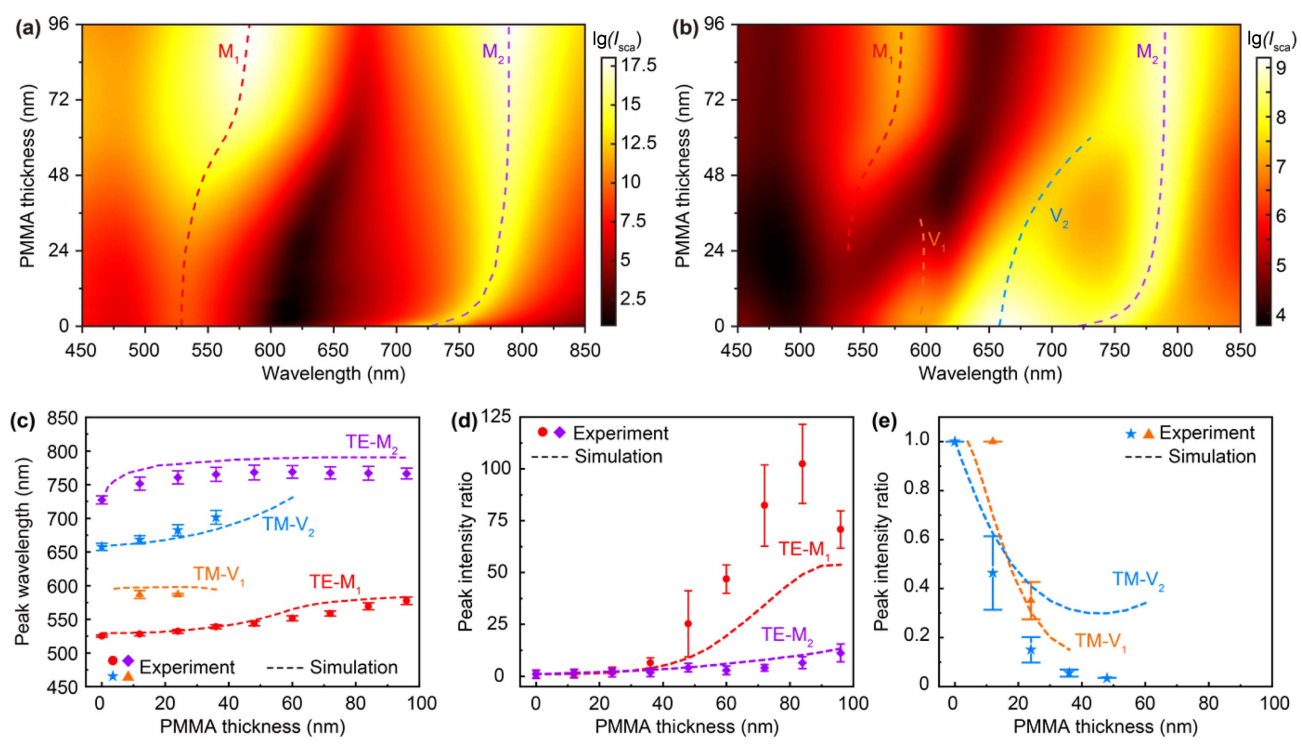


Fig. 3. Statistical analysis of plasmonic resonances of NCoM nanocavity embedded in PMMA layer with varied thickness. (a), (b) Numerically calculated scattering spectra of an NCoM plasmonic nanocavity embedded in a PMMA layer with a varied thickness under TE (a) and TM (b) excitation conditions. For better readability, the scattering intensities are presented in a logarithmic scale. The dashed lines indicate the resonance wavelengths of modes M_1 (red lines), V_1 (orange lines), V_2 (blue lines), and M_2 (purple lines). (c) Resonance wavelengths for the plasmonic modes obtained from experiments (solid dots) and simulations (dashed lines) for various thicknesses of the PMMA layer. (d), (e) Peak intensity ratio for modes M_1 and M_2 under TE excitation (d) and modes V_1 and V_2 under TM excitation (e) derived from the experimental measurements (solid dots) and simulations (dashed lines) for various thicknesses of the PMMA layer.

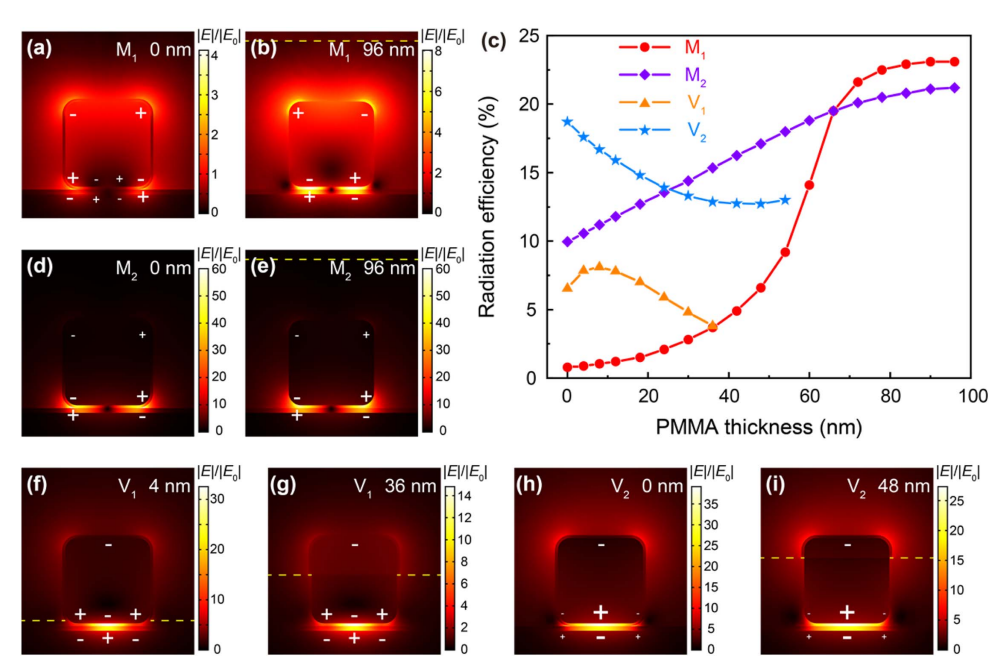


Fig. 4. Numerical simulations of excitation and radiation efficiencies of NCoM nanocavities. (a), (b) Numerically simulated near-field distributions of an electric field in the yz-plane corresponding to nanocavity modes M_1 for the nanocavity without (a) and with the PMMA layer (b). (c) Numerically simulated radiation efficiency for modes M_1 (red line), M_2 (purple line), V_1 (orange line), and V_2 (blue line) obtained using an eigen-frequency solver, for nanocavities with varied thickness of the PMMA layer. (d)–(i) Numerically simulated near-field distributions of an electric field in the yz-plane corresponding to nanocavity modes M_2 (d), (e), V_1 (f), (g) and V_2 (h), (i) for the nanocavity with varied thickness of the PMMA layer.

reaches its maximum value of $\sim 11\pm 4$ in the experiment and ~ 10 in the simulations at the PMMA thickness of 96 nm [Fig. 3(d)]. This shows that for mode M_2 , which is strongly localized in the nanocavity gap for all the PMMA thicknesses [Figs. 4(d) and 4(e)], the retardation has a negligible effect on the excitation efficiency. Comparing the overall scattering enhancement with the radiative counterpart [increasing from 9.9% to 21.2% as d_p increases from 0 to 96 nm, Fig. 4(c)], one can conclude that for mode M_2 the excitation and radiation enhancements have comparable contributions.

In dramatic contrast to the in-plane modes M_1 and M_2 , the evolution in the peak scattering intensities of the out-of-plane modes V₁ and V₂ shows the opposite behavior. Particularly, mode V₁ keeps its resonant wavelength around 598 nm with the increase of d_p from 0 to 36 nm [orange lines in Fig. 3(c)], while its peak intensity decreases gradually [Fig. 3(e)]. Mode V₂, which dominates the scattering spectrum of the nanocavity under the TM-polarized illumination in the absence of the PMMA layer, undergoes a progressive red-shift from 660 to 726 nm with the increase of d_p from 0 to ~48 nm [blue lines in Fig. 3(c)] and then spectrally overlaps with mode M2. At the same time, its peak intensity dramatically decreases to a nearly zero value [Fig. 3(e)]. According to the theoretic calculation results, with the increase of d_p from 0 to 36 nm, there is ~4 and 1.7 times decrease in the mode local intensity [Figs. 4(f) and 4(g)] and radiation efficiency [Fig. 4(c)] for mode V₁, which indicates that the decrease of the excitation and radiation efficiencies plays a comparable role in the overall effect. Comparing the corresponding quantities for mode V₂ [Figs. 4(c), 4(h), and 4(i)], one can also conclude that in this case the reductions of excitation (~2 times decrease) and radiation (~1.5 times decrease from 18.7% to 12.7%) efficiencies have comparable contributions.

4. CONCLUSION

By embedding NCoM plasmonic nanocavities into a PMMA layer with a controllable thickness, we have demonstrated

selective excitation of their plasmonic resonances, achieving a scattering intensity enhancement up to ~102 times for the normally dark in-plane plasmonic modes. This can be exploited for enhancing interaction of light with in-plane oriented matter states at the atomic scale. The main advantage of this approach is that the deposition and etching of the PMMA layer have negligible effects on both the nanocavity structure and functional materials frequently integrated in the nanocavity gap, enabling robust engineering and enhancement of light-matter interactions at the atomic scale. More interestingly, the insulating PMMA layer with a precisely controllable thickness partially surrounding nanoparticles opens a prospective for electric connection with nanoparticles featuring a sub-100 nm footprint [18,39-41]. Moreover, if the embedding medium PMMA is replaced with a humidity-sensitive polymer, it can undergo refractive index and volume changes in response to ambient humidity [42,43]. This, in turn, alters the plasmonic resonances of the nanocavity, offering a promising route toward optical humidity sensing with high sensitivity and high spatial resolution. Overall, the demonstrated approach for plasmonic mode manipulation through highly controllable embedding of plasmonic nanostructures into dielectric nanolayers provides a universal platform for the enhancement of light-matter interactions and opens opportunities for improving the performance of nanophotonic and quantum devices.

APPENDIX A: FABRICATION OF DIELECTRIC-EMBEDDED NCOM PLASMONIC NANOCAVITIES

The procedure for the fabrication of the dielectric-embedded NCoM plasmonic nanocavities is schematically shown in Fig. 5. Firstly, a single-crystal gold flake with a thickness of 50 nm was synthesized on a glass slide [Fig. 5(a)] [19]. Secondly, a 2.5-nm-thick alumina layer was deposited on the surface of the gold flake using molecular-assisted atomic layer deposition to produce a dielectric spacer [Fig. 5(b)] [19]. Thirdly, a diluted solution of gold nanocubes was drop-casted onto the gold flake to define the plasmonic nanocavities

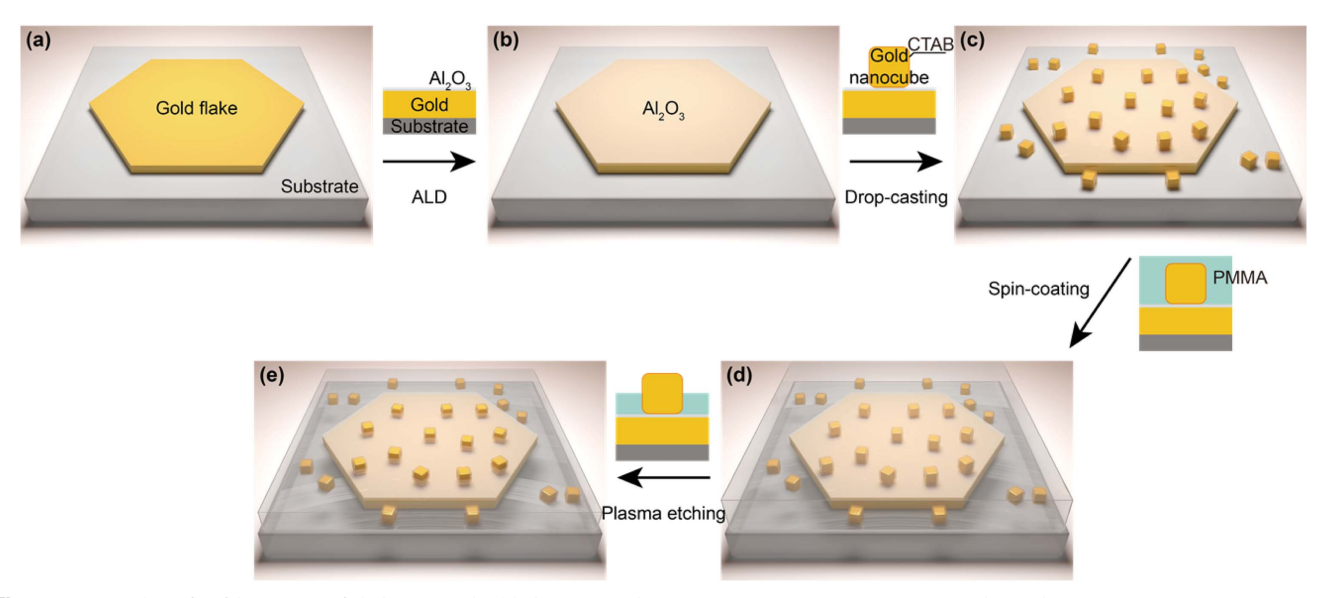


Fig. 5. Procedure for fabrication of dielectric-embedded NCoM plasmonic nanocavities. ALD, atomic layer deposition.

[Fig. 5(c)]. Fourthly, a PMMA layer (950A2, MicroChem) was spin-coated onto the sample [Fig. 5(d)], which was subsequently baked at 120°C for 3 min. It has a thickness of \sim 96 nm, which is controlled by spin-coating parameters (500 r/min for 5 s first and then followed by 3500 r/min for 50 s) of PMMA solution. Finally, the PMMA layer was partially etched with O₂ plasma to tune its thickness by controlling the etching time [Fig. 5(e)]. The O₂ plasma etching was operated under a very mild condition with a plasma power of 30 W, gas flow rate of 600 sccm, and chamber pressure of 40 Pa.

APPENDIX B: TEM CHARACTERIZATION

For cross-sectional TEM characterization of the NCoM plasmonic nanocavities without a PMMA layer, an electron-transparent cross-sectional lamella of a selected nanocavity was prepared as follows. Firstly, NCoM plasmonic nanocavities were fabricated on a glass substrate using the approach introduced in Appendix A. Secondly, a layer of carbon (~150 nm in thickness) was sputtered on the sample to protect the nanocavities. Then, an NCoM plasmonic nanocavity was selected under SEM imaging, and a cross-sectional lamella of the nanocavity with a thickness of ~100 nm was obtained using focused-ion-beam (FIB) milling (Helios G4, Thermo Scientific). Finally, the lamella was transferred onto a copper grid and imaged using a high-resolution transmission electron microscope (F200X G2, Talos) operated at 200 kV.

APPENDIX C: DARK-FIELD SPECTROSCOPY SETUP

The setup for the measurement of dark-field scattering from the NCoM plasmonic nanocavities is schematically shown in Fig. 6(a). A TE- or TM-polarized beam from a supercontinuum white light laser (FIU-6, NKT Photonics) was first focused onto the nanocavities at an oblique incidence angle of about 80° with respect to the surface normal. The scattering signal from individual nanocavities was first collected by a $100\times$ objective (NA = 0.9, TU Plan Fluor, Nikon), and then directed using a beam splitter to a CCD camera (DS-Fi3, Nikon) for imaging and to a spectrometer (QE Pro, Ocean Optics) for the spectral analysis. All measured scattering spectra were normalized by the spectrum of the supercontinuum white light laser and the spectral response of the detection system.

The actual spectral collection region of the setup can be characterized by sending a white light into the optical fiber and then imaging the focused light on the object plane, as shown in Fig. 6(b). The yellow spot clearly shows the spectral collection region, which has a diameter of \sim 875 nm in the object plane.

APPENDIX D: NUMERICAL SIMULATIONS

Numerical simulations of the dielectric-embedded plasmonic nanocavities were performed using a finite element method (COMSOL Multiphysics software). The geometry of the NCoM plasmonic nanocavity used for the simulations, schematically shown in Fig. 7, was set to match that of the experimentally measured structures (derived from cross-sectional TEM images). The refractive index of the single-crystal gold was taken from Ref. [44]. The refractive indices of the glass substrate, alumina, CTAB, and PMMA were set to be 1.45, 1.70, 1.44, and 1.48, respectively.

The dark-field scattering spectra were modeled in the scattering formulation. The nanocavity was illuminated with a TE- or TM-polarized electromagnetic plane wave at 80° to match the experimental conditions. The wavelength of the incident wave was varied from 450 to 850 nm, while the power flow of the scattered fields was integrated inside a 64° collection

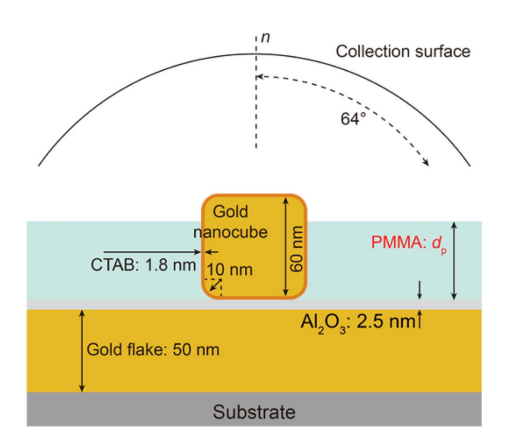


Fig. 7. Schematic illustration of the model used for numerical simulations of the scattering spectra, surface charge density distributions, and eigen-frequency of nanocube-on-mirror plasmonic nanocavites.

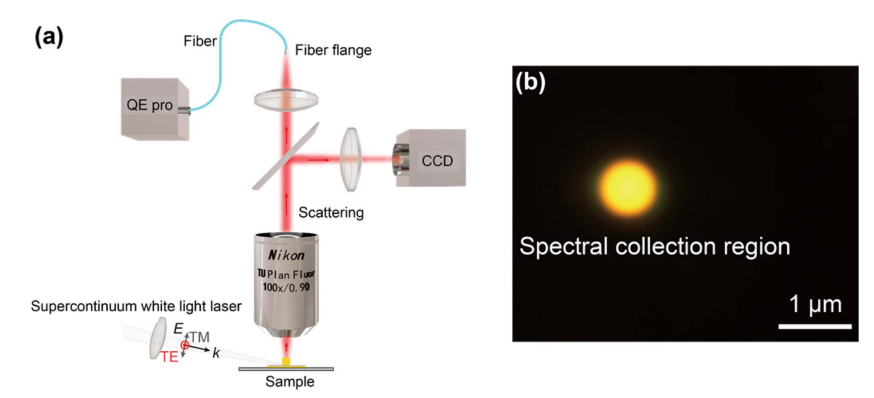


Fig. 6. (a) Dark-field spectroscopy setup. (b) Optical micrograph of spectral collection region on the object plane.

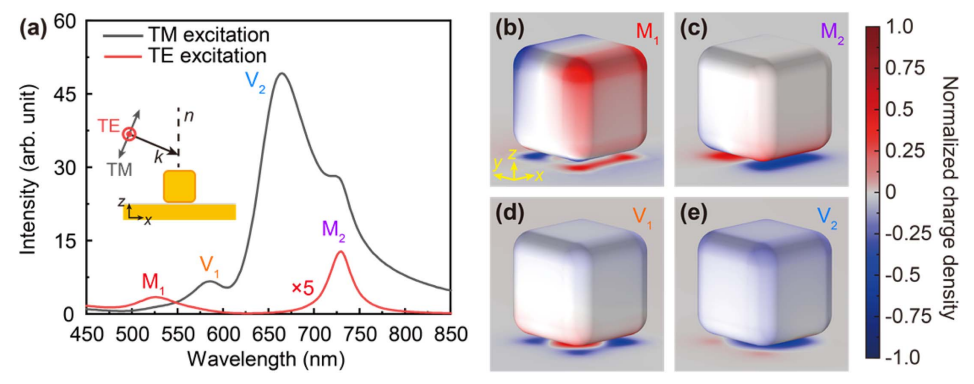


Fig. 8. (a) Numerically simulated scattering spectra under TM- or TE-polarized excitation (note that the TE signal was magnified by five times). (b)–(e) Normalized charge density distributions on the surfaces of the gold nanocube and flake corresponding to the plasmonic modes (b) M_1 , (c) M_2 , (d) V_1 , and (e) V_2 labeled in (a).

angle corresponding to the NA of the objective employed in the experiments, 2.5 μ m from the center of the nanocube bottom face. The calculated scattering spectra are shown in Fig. 8(a). The normalized surface charge density distributions (ρ) of the plasmonic modes labeled in Fig. 8(a) were obtained from the full vectorial field given by the numerical solutions [Figs. 8(b)–8(e)]. The electric near-field distributions ($|E|/|E_0|$) for various modes of the dielectric-embedded NCoM plasmonic nanocavities with a varied thickness of the PMMA layer were obtained as well, as shown in Figs. 4(a), 4(b), and 4(d)–4(i). Eigenmode simulations were performed using a built-in eigenfrequency solver; the results are shown in Fig. 4(c).

APPENDIX E: MEASURED THICKNESS-ETCHING TIME CORRELATION CURVE

To accurately determine the thickness-etching time correlation curve, we created a step edge in the initial PMMA layer by gently scoring it with a surgical blade after spin-coating [Fig. 9(a)], and measured the step height using a stylus profilometer (Bruker DEKTAK-XT) for different etching times [Fig. 9(b)]. We performed this measurement across 10 different samples to establish a reliable correlation between the PMMA thickness and etching time [Fig. 2(b)].

APPENDIX F: STABILITY OF THE NANOCAVITIES UNDER SPIN-COATING AND ETCHING OF PMMA LAYER

To characterize the stability of nanocavities under the spincoating and etching of the PMMA layer, a sample containing many nanocavities on a gold flake was first fabricated, and then three rounds of spin-coating of the PMMA layer and complete plasma etching were performed. During the test, the positions of the nanocavities during each step were recorded using dark-field scattering microscopy. As shown in Fig. 10(a), due to the strong attraction between the gold nanocube and flake with an ultrasmooth face contact, the relative positions of the nanocavities remained unchanged after the multi-round spin-coating and etching of the PMMA layer. Furthermore, we performed a plasma etching-stability experiment with the NCoM nanocavities. The scattering spectrum of an NCoM nanocavity was first recorded before spin-coating the PMMA layer for reference [black line in Fig. 10(b)]. Then, the PMMA layer was etched for 160 s by O₂ plasma to completely remove the PMMA layer. The exposed nanocavity was further etched by plasma for another 160 s to test its stability. The scattering spectra taken after plasma etching for 160 s [red line in Fig. 10(b)] and 320 s [blue line in Fig. 10(b)] are nearly identical with the original one, confirming that

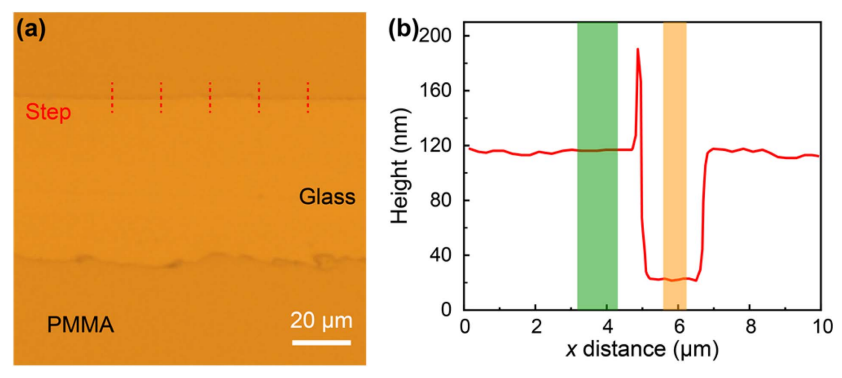


Fig. 9. (a) Optical micrograph of a PMMA layer with an initial thickness of ~96 nm, which was gently scored by a surgical blade after spin-coating. The red dashed lines represent the scanning path for measuring the step height with a stylus profilometer. (b) Example of measured step height profile corresponding to the scan path in (a). The final step height is obtained by averaging the five measured heights.

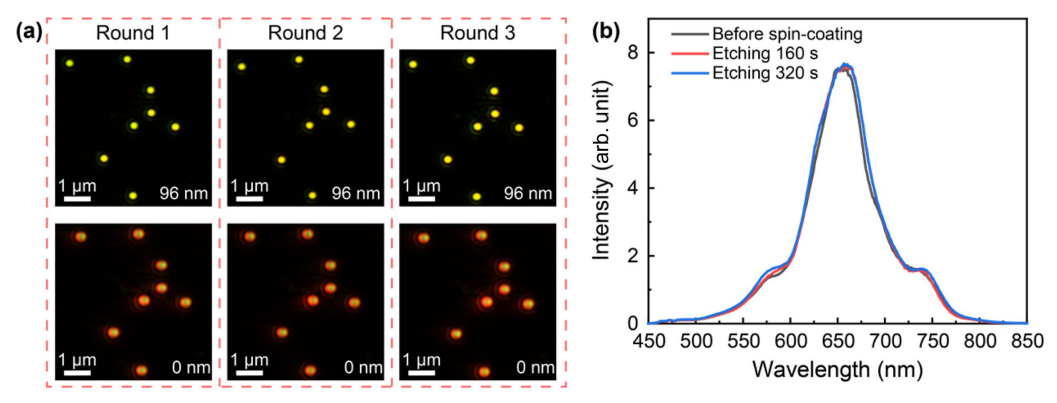


Fig. 10. (a) Dark-field scattering images of NCoM nanocavities with or without PMMA layer taken under TM excitation condition for multiround spin-coating and etching, showing consistent relative positions. (b) Scattering spectra from an NCoM nanocavity measured before spin-coating of PMMA layer (black line), after etching for 160 s (the PMMA layer has been completely removed, red line) and 320 s (blue line) under TM excitation.

applying the O_2 plasma etching has a negligible effect on the structure and optical response of the nanocavities.

Funding. National Key Research and Development Program of China (2023YFB2806701); National Natural Science Foundation of China (92250305, 62305293); Natural Science Foundation of Zhejiang Province (LR25F050001, LDT23F04015F05); Engineering and Physical Sciences Research Council (EP/W017075/1); New Cornerstone Science Foundation (NCI202216).

Disclosures. The authors declare no conflicts of interest.

Data Availability. Data underlying the results presented in this paper are not publicly available at this time but may be obtained from the authors upon reasonable request.

REFERENCES

- D. K. Gramotnev and S. I. Bozhevolnyi, "Plasmonics beyond the diffraction limit," Nat. Photonics 4, 83–91 (2010).
- A. V. Zayats, I. I. Smolyaninov, and A. A. Maradudin, "Nano-optics of surface plasmon polaritons," Phys. Rep. 408, 131–314 (2005).
- S. Lal, S. Link, and N. J. Halas, "Nano-optics from sensing to waveguiding," Nat. Photonics 1, 641–648 (2007).
- 4. J. N. Anker, W. P. Hall, O. Lyandres, et al., "Biosensing with plasmonic nanosensors," Nat. Mater. 7, 442–453 (2008).
- N. Liu, M. L. Tang, M. Hentschel, et al., "Nanoantenna-enhanced gas sensing in a single tailored nanofocus," Nat. Mater. 10, 631–636 (2011).
- H. Xu, E. J. Bjerneld, M. Käll, et al., "Spectroscopy of single hemoglobin molecules by surface enhanced Raman scattering," Phys. Rev. Lett. 83, 4357–4360 (1999).
- P. Wang, A. V. Krasavin, L. Liu, et al., "Molecular plasmonics with metamaterials," Chem. Rev. 122, 15031–15081 (2022).
- 8. X. X. Han, R. S. Rodriguez, C. L. Haynes, et al., "Surface-enhanced Raman spectroscopy," Nat. Rev. Methods Primers 1, 87 (2022).
- R. F. Oulton, V. J. Sorger, T. Zentgraf, et al., "Plasmon lasers at deep subwavelength scale," Nature 461, 629–632 (2009).
- M. Ayata, Y. Fedoryshyn, W. Heni, et al., "High-speed plasmonic modulator in a single metal layer," Science 358, 630–632 (2017).
- C. Ciracì, R. Hill, J. Mock, et al., "Probing the ultimate limits of plasmonic enhancement," Science 337, 1072–1074 (2012).

- G.-C. Li, Q. Zhang, S. A. Maier, et al., "Plasmonic particle-onfilm nanocavities: a versatile platform for plasmon-enhanced spectroscopy and photochemistry," Nanophotonics 7, 1865–1889 (2018).
- J. J. Baumberg, J. Aizpurua, M. H. Mikkelsen, et al., "Extreme nanophotonics from ultrathin metallic gaps," Nat. Mater. 18, 668–678 (2019).
- Z. Lu, J. Ji, H. Ye, et al., "Quantifying the ultimate limit of plasmonic near-field enhancement," Nat. Commun. 15, 8803 (2024).
- R. Chikkaraddy, B. de Nijs, F. Benz, et al., "Single-molecule strong coupling at room temperature in plasmonic nanocavities," Nature 535, 127–130 (2016).
- N. Rivera, I. Kaminer, B. Zhen, et al., "Shrinking light to allow forbidden transitions on the atomic scale," Science 353, 263–269 (2016).
- H. Chen, Z. Jiang, H. Hu, et al., "Sub-50-ns ultrafast upconversion luminescence of a rare-earth-doped nanoparticle," Nat. Photonics 16, 651–657 (2022).
- J. Zheng, A. V. Krasavin, R. Yang, et al., "Active control of excitonic strong coupling and electroluminescence in electrically driven plasmonic nanocavities," Sci. Adv. 11, eadt9808 (2025).
- L. Liu, A. V. Krasavin, J. Zheng, et al., "Atomically smooth singlecrystalline platform for low-loss plasmonic nanocavities," Nano Lett. 22, 1786–1794 (2022).
- Z. Wang, L. Liu, D. Zhang, et al., "Effect of mirror quality on optical response of nanoparticle-on-mirror plasmonic nanocavities," Adv. Opt. Mater. 11, 2201914 (2023).
- K. J. Russell, T.-L. Liu, S. Cui, et al., "Large spontaneous emission enhancement in plasmonic nanocavities," Nat. Photonics 6, 459– 462 (2012).
- G. M. Akselrod, C. Argyropoulos, T. B. Hoang, et al., "Probing the mechanisms of large Purcell enhancement in plasmonic nanoantennas," Nat. Photonics 8, 835–840 (2014).
- C. Awada, T. Popescu, L. Douillard, et al., "Selective excitation of plasmon resonances of single Au triangles by polarization-dependent light excitation," J. Phys. Chem. C 116, 14591–14598 (2012).
- D. Zheng, S. Zhang, Q. Deng, et al., "Manipulating coherent plasmonexciton interaction in a single silver nanorod on monolayer WSe₂," Nano Lett. 17, 3809–3814 (2017).
- R. Esteban, G. Aguirregabiria, A. G. Borisov, et al., "The morphology of narrow gaps modifies the plasmonic response," ACS Photonics 2, 295–305 (2015).
- S. Huang, T. Ming, Y. Lin, et al., "Ultrasmall mode volumes in plasmonic cavities of nanoparticle-on-mirror structures," Small 12, 5190–5199 (2016).
- C. Tserkezis, R. Esteban, D. O. Sigle, et al., "Hybridization of plasmonic antenna and cavity modes: extreme optics of nanoparticle-on-mirror nanogaps," Phys. Rev. A 92, 053811 (2015).

- J.-W. Jeon, J. Zhou, J. A. Geldmeier, et al., "Dual-responsive reversible plasmonic behavior of core-shell nanostructures with pH-sensitive and electroactive polymer shells," Chem. Mater. 28, 7551–7563 (2016).
- X. Han, Z. He, D. Zhao, et al., "Real-time tuning exciton-plasmon coupling with photosensitive nanocavity," Adv. Opt. Mater. 12, 2301553 (2024)
- J.-E. Park, Y. Lee, and J.-M. Nam, "Precisely shaped, uniformly formed gold nanocubes with ultrahigh reproducibility in single-particle scattering and surface-enhanced Raman scattering," Nano Lett. 18, 6475–6482 (2018).
- C. Pan, Y. Tong, H. Qian, et al., "Large area single crystal gold of single nanometer thickness for nanophotonics," Nat. Commun. 15, 2840 (2024).
- D. Y. Lei, A. I. Fernández-Domínguez, Y. Sonnefraud, et al., "Revealing plasmonic gap modes in particle-on-film systems using dark-field spectroscopy," ACS Nano 6, 1380–1386 (2012).
- G.-C. Li, Y.-L. Zhang, and D. Y. Lei, "Hybrid plasmonic gap modes in metal film-coupled dimers and their physical origins revealed by polarization resolved dark field spectroscopy," Nanoscale 8, 7119– 7126 (2016).
- Q. Zhang, G. C. Li, T. W. Lo, et al., "Polarization-resolved optical response of plasmonic particle-on-film nanocavities," J. Opt. 20, 024010 (2018)
- H. Sugimoto, S. Yashima, and M. Fujii, "Hybridized plasmonic gap mode of gold nanorod on mirror nanoantenna for spectrally tailored fluorescence enhancement," ACS Photonics 5, 3421–3427 (2018).

- R. Chikkaraddy, J. Huang, D. Kos, et al., "Boosting optical nanocavity coupling by retardation matching to dark modes," ACS Photonics 10, 493–499 (2023).
- M. G. Nielsen, A. Pors, R. B. Nielsen, et al., "Demonstration of scattering suppression in retardation-based plasmonic nanoantennas," Opt. Express 18, 14802–14811 (2010).
- N. Kongsuwan, A. Demetriadou, M. Horton, et al., "Plasmonic nanocavity modes: from near-field to far-field radiation," ACS Photonics 7, 463–471 (2020).
- D. Kos, D. R. Assumpcao, C. Guo, et al., "Quantum tunneling induced optical rectification and plasmon-enhanced photocurrent in nanocavity molecular junctions," ACS Nano 15, 14535–14543 (2021).
- J. Huang, S. Hu, D. Kos, et al., "Enhanced photocurrent and electrically pumped quantum dot emission from single plasmonic nanoantennas," ACS Nano 18, 3323–3330 (2024).
- S. Hu, J. Huang, R. Arul, et al., "Robust consistent single quantum dot strong coupling in plasmonic nanocavities," Nat. Commun. 15, 6835 (2024).
- M. A. C. Stuart, W. T. S. Huck, J. Genzer, et al., "Emerging applications of stimuli-responsive polymer materials," Nat. Mater. 9, 101–113 (2010).
- J. Yoon, C. Jung, J. Kim, et al., "Chemically and geometrically programmable photoreactive polymers for transformational humiditysensitive full-color devices," Nat. Commun. 15, 6470 (2024).
- R. L. Olmon, B. Slovick, T. W. Johnson, et al., "Optical dielectric function of gold," Phys. Rev. B 86, 235147 (2012).